Supplementary Information (SI) for Physical Chemistry Chemical Physics.

Electronic Supplementary Information

Formation of HNC and HCN isomers in molecular plasmas revealed by frequency comb and quantum cascade laser spectroscopy

Ibrahim Sadiek,*[a] Simona Di Bernardo,[a,c,d] Uwe Macherius[b] and Jean-Pierre H. van Helden[a]

[a]*Experimental Physics V: Spectroscopy of Atoms and Molecules by Laser Methods, Faculty of Physics and Astronomy, Ruhr University Bochum, 44780 Bochum, Germany*

[b]*Leibniz Institute for Plasma Science and Technology (INP), 17489 Greifswald, Germany*

[c]*Department of Mathematics and Physics, University of Campania "Luigi Vanvitelli", 81100 Caserta, Italy*

[d]*Italian Aerospace Research Centre (CIRA), 81043 Capua, Italy*

Content:

A. The EC-QCL spectrometer

(i) Experimental details

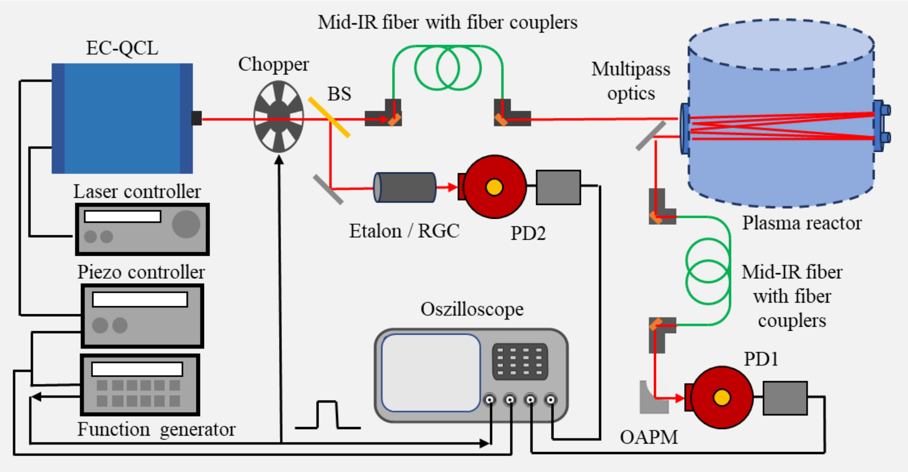

Fig. S1. Overview schematic of the experimental setup of the EC-QCL absorption spectrometer. Two liquid nitrogen-cooled photodetectors (PD1 and PD2) were used for the signal and reference measurements, respectively. The laser light was coupled into mid-IR fibers, directed through multi-pass optics connected to the reactor, and then to PD1. An etalon and CO or CO_2 reference gas cells (RGC) were used for wavenumber calibration. An off-axis optical parabolic mirrors (OAPM) were used in front of PD1.

The experimental setup of the external-cavity quantum cascade laser (EC-QCL) absorption spectrometer is shown in Fig. S1. A plasma reactor (Rübig) equipped with a multi-pass optics with BaF_2 windows (neoplas control) was used for *in situ* absorption measurements. Gas flows were regulated using mass flow controllers (with MKS MFCs of 1259CJ-00020RV type for H_2 and N_2, and 1259CC-00050RV for CH_4). The reactor pressure was stabilized at 1 mbar via a back pressure controller connected to a vacuum pump. The reactor's outer wall was water-cooled at (293.0 ± 0.1) K using a recirculating chiller, resulting in a stabilized internal wall temperature of (295 ± 1) K. Temperatures were monitored using two thermocouples placed on the inner wall, and a third thermocouple recorded the gas temperature near a stainless-steel blank working load. The plasma was generated by direct current (dc) discharge under gas flows of 11 sccm N_2, 1 sccm H_2, and 8 sccm CH_4 and a plasma power of 700 W at 1 mbar.

A continuous-wave EC-QCL (Daylight Solutions 21047-MHF-011), with an output power exceeding 150 mW, was used as a light source. The full wavenumber tunability of the laser was 1985 – 2250 cm^{-1}, and here it was scanned across the 2069 – 2087 cm^{-1} range within its mode-hop free range. Coarse spectral tuning was achieved by rotating the external grating using a stepper motor, while high-resolution scans across ~1 cm^{-1} were performed using a piezoelectric transducer (PZT) attached to the grating, modulated by a sine wave at 80 Hz generated by a function generator (Agilent Technologies, HP 33120A) and amplified using one channel of a three-channel PZT controller (Thorlabs MDT693A). The PZT drive signal was swept from 0 to 80 V, enabling fine-tuned frequency sweeps for high spectral resolution measurements.

A linear polarizer was used as a power attenuator and a beam splitter to couple the back reflected part of the laser power into the reference channel. Further attenuation of the laser power was achieved using irises in the beam path. After attenuation, the laser beam was coupled into a single-mode mid-infrared (mid-IR) fiber (Thorlabs) for beam cleaning, as well as to simplify the optical setup and enhance its robustness, before being directed to the plasma reactor. The transmitted light was collected by another mid-IR fiber and focused on an off-axis optical parabolic mirror (OAPM), placed in front of a liquid nitrogen (LN_2)-cooled MCT detector PD1 (Judson, J15D12-M204-S01M-60, with a 1 MHz bandwidth preamplifier, PB 101). The signal was recorded by a 440 MHz PC-based oscilloscope (Lecroy WaveRunner 44MXi-A), which simultaneously acquired data from the signal, etalon, and reference channels.

(ii) Measurements procedure and frequency calibration

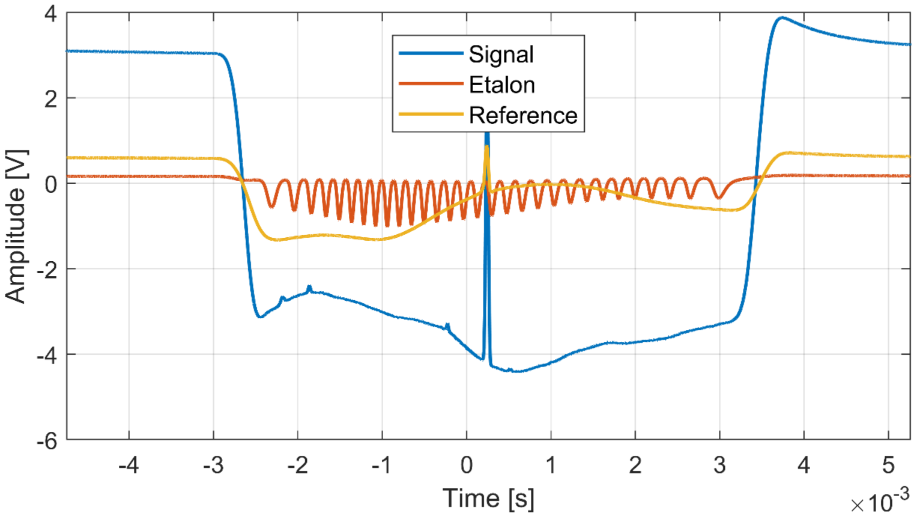

Fig. S2. Raw data of measured spectra for the signal channel (with PD1) and reference (RGC with 1 mbar of CO) and etalon (both with PD2) using the EC-QCL setup.

Fig. S2 presents a representative measurement of the etalon, signal and reference spectra, using the EC-QCL setup. The laser was scanned over approximately 1.0 cm^{-1}. For relative frequency calibration, a germanium etalon (free spectral range of 0.04881cm^{-1}) was used in the reference arm. Approximately 10% of the laser power was directed through the etalon, and the resulting interference fringes were detected by the LN_2- cooled detector PD2 (Judson, J15D22-M204-S01M-60-ZnSe, with a 1 MHz bandwidth preamplifier PB 101).

Although the schematic shown in Fig. S1 depicts two optical beam paths, three different signal traces are shown in Fig. S2: the plasma transmission (absorption) signal, an etalon signal used for relative frequency calibration, and a reference gas spectrum. The etalon and reference signals were acquired using the same reference arm and are not measured simultaneously. Instead, the etalon or the reference gas cell is alternately inserted into the reference arm. Indeed, a dedicated etalon measurement was not required for each experimental run. Earlier versions of the spectrometer employed a third arm for simultaneous acquisition; however, this arm was removed in the present configuration to simplify the setup.

The averaged spectra (1000 averages) were processed as follows: (i) the background was subtracted such that the baseline of the signal (with the chopper closed) was set to zero; (ii) spectral calibration was performed using the etalon data, by fitting a 5th-order polynomial to the fringe maxima and using known CO or CO_2 absorption lines in the 2069–2087 cm^{-1} range for absolute calibration; (iii) the absorption features were masked, and a 9th-order polynomial was used to fit the remaining baseline; (iv) the signal was then divided by the fitted baseline to obtain the transmission spectrum; and (v) the absorption spectrum was calculated as the natural logarithm of the transmission signal. This final absorption spectrum was then used to determine the population of rotational and vibrational states of HNC and HCN.

B. Determination of HCN and HNC populations

The final absorption spectrum measured by the comb was used to retrieve individual rotational level populations across three vibrational bands of HCN. Similarly, the spectra measured by the EC-QCL setup were used to determine the populations of HNC and HCN, based on one line for the former and two for the latter (see Fig. 3 in the main text). For the population determination, we follow a line-by-line analysis approach,[1] where each absorption profile is fitted using a Gaussian line-shape model, with Doppler width and line center were treated as free parameters. Only well-resolved absorption profiles with a minimum signal-to-noise ratio of ~10 were included, and saturated profiles were excluded. Saturation is particularly evident for the low-J transitions of the ν_1 band of HCN (Figure 2a), which were therefore not used for population determination. The remaining unsaturated lines provided sufficient information to construct Boltzmann plots, extrapolate populations for unmeasured levels, and reliably determine rotational and vibrational populations. The population in a rotational level, n_{j}, can be expressed in terms of the experimental observables, incident $I_0(\tilde{\nu})$ and transmitted $I(\tilde{\nu})$ intensities:

$$n_j = \left(\frac{g_{\mathrm{j}}}{g_{\mathrm{k}}} \cdot \frac{8\pi c \tilde{\nu}_{\mathrm{jk}}^2}{A_{jk}}\right) \cdot \frac{1}{L} \cdot \int \ln\left(\frac{I_0(\tilde{\nu})}{I(\tilde{\nu})}\right) d\tilde{\nu}, \tag{1}$$

where g_{j} and g_{k} are the statistical weights of the lower and upper states, respectively, A_{jk} is the Einstein coefficient for spontaneous emission, and L is the optical path length. Note that Eq. 1 simplifies $\left(n_j \cdot \frac{g_{\mathrm{k}}}{g_j} - n_{\mathrm{k}}\right) \approx n_j \cdot \frac{g_k}{g_j}$, which is valid when $n_j \gg n_k$. This holds true up to ~1000 K (comparable to the observed vibrational temperature here), where $n_k/n_j \approx \exp(-\,3300/(k_{\mathrm{B}}T) = 0.0087$, with k_{B} = 0.6950356 cm^{-1} is the Boltzmann constant. For lower transition frequencies (< 1000 cm^{-1}), this simplification might be critical, particularly under non-equilibrium plasma conditions.

Under local thermodynamic equilibrium (LTE), the rotational level populations within a vibrational state ν (which still doesn't have to be in thermal equilibrium with other vibrational states)[2] follows a Boltzmann distribution:

$$n_j = n_\nu \cdot \phi(J;\, T_{\mathrm{rot}}), \tag{2}$$

where the rotational population fraction is:

$$\phi(J;\, T) = \frac{(2J+1)\cdot \exp\left(-E_{\mathrm{j}}/k_{\mathrm{B}}T_{\mathrm{rot}}\right)}{Q(T_{\mathrm{rot}})}. \tag{3}$$

Here, $2J+1$ is the rotational degeneracy for levels with rotational quantum number J, and $Q(T_{\mathrm{rot}})$ is the rotational partition function including the state dependent and independent degeneracies, g_{s} and g_{in}, respectively:[3]

$$Q(T_{\mathrm{rot}}) = \sum_{J=0}^{J_{\max}} (2J+1) \cdot g_{\mathrm{s}} \cdot g_{\mathrm{in}} \cdot \exp\left(-\frac{E_J}{k_{\mathrm{B}}T_{\mathrm{rot}}}\right) \tag{4}$$

However, under the non-equilibrium conditions of plasma, our observed populations of HCN deviate from a single-temperature Boltzmann distribution, showing clear non-LTE behavior. The data show two distinct slopes in a semi-logarithmic plot of $\ln(n_j/g_{\mathrm{j}})$ versus lower state energy, E_J, indicative of a bi-modal temperature distribution, see Fig. 2c of the main text.

These non-LTE rotational populations were therefore modeled using a segmented two-temperature approach, where two rotational temperatures, $T_{\mathrm{rot},1}$ and $T_{\mathrm{rot},2}$ were extracted by fitting linear segments to the data in $\ln(n_j/g_j)$ vs. E_J, with an optimally determined crossing rotational quantum number, J_{cross}, that maximizes the overall R^2 of the two linear fits.

The rotational population distribution within a vibrational state is then modelled as:

$$n_j = \begin{cases} n_{v,1} \cdot \dfrac{(2J+1)\cdot \exp\left(-E_J/k_B T_{\mathrm{rot},1}\right)}{Q\left(T_{\mathrm{rot},1}\right)}, & J < J_{cross} \\ n_{v,2} \cdot \dfrac{(2J+1)\cdot \exp\left(-E_J/k_B T_{\mathrm{rot},2}\right)}{Q\left(T_{\mathrm{rot},2}\right)}, & J \geq J_{cross} \end{cases} \tag{5}$$

Here, $n_{v,1}$ and $n_{v,2}$ represent the vibrational state populations associated with the lower- and higher-J segments, respectively. $Q(T_{\mathrm{rot},1})$ and $Q(T_{\mathrm{rot},2})$ are rotational partition functions, evaluated over the corresponding J-ranges (for $Q(T_{\mathrm{rot},1})$ the summation goes up to (J_{cross} −1), while for $Q(T_{\mathrm{rot},2})$ the summation goes from J_{cross} to a $J_{\max}$ of 60) using respective $T_{\mathrm{rot},1}$ and $T_{\mathrm{rot},2}$, determined from the linear fits. For the evaluation of the rotational partition sums, we used the improved line lists[4] for both HCN and HNC isomers in the ExoMol database.[5]

Table S1 lists the obtained rotational temperatures from the segmented linear fit around J_{cross}, together with the determined populations of vibrational states according to Eq. 5 for three vibrational states of HCN. The determined populations of vibrational states, n_v, are used together with the vibrational degeneracies, g_v, to determine vibrational temperatures of 01^10 and 02^00 states. From the linear fit of $\ln(n_v/g_v)$ vs. vibrational energies we evaluated from the slope of the fit a vibrational temperature of 993 ± 68 K.

Uncertainties in rotational temperatures $T_{\mathrm{rot},1}$, and $T_{\mathrm{rot},2}$ are evaluated from the slope uncertainties obtained from the weighted least-squares fits as $\delta T_{\mathrm{rot}} = |T_{\mathrm{rot}} \cdot \delta slope/slope|$. The population constants $C1$ = exp(intercept1) and $C2$=exp(intercept2), propagate their errors through $\delta C = C \cdot \delta\mathrm{intercept}$. The vibrational state populations $n_{v,1} = \mathrm{C1} \cdot Q(T_{\mathrm{rot},1})$ and $n_{v,2} = \mathrm{C2} \cdot Q(T_{\mathrm{rot},2})$ include uncertainties from both the intercept and from the temperature dependence of the partition function $Q(T_{\mathrm{rot}})$. The latter has a minor contribution, and it was quantified by numerically differentiating the interpolated $Q(T_{\mathrm{rot}})$ near rotational temperatures obtained from the linear fit.

Table S1. The extracted rotational temperatures $T_{\mathrm{rot},1}$ and $T_{\mathrm{rot},2}$ from the segmented fitting approach at optimal J_{cross}, as well as the determined populations of vibrational states of HCN.

State	$T_{\mathrm{rot},1}$; $T_{\mathrm{rot},2}$ [K]	ΔT_{rot}[K]	J_{cross}	$n_{v,1}$; $n_{v,2}$ [10^{15} cm^{-3}]	n_v [10^{15} cm^{-3}]
00^00	357 ± 4; 488 ± 5	131	18	2.667 ± 0.040; 1.887 ± 0.081	4.554 ± 0.090
01^10	436 ± 4; 535 ± 7	99	21	2.081 ± 0.063; 0.795 ± 0.052	2.876 ± 0.082
02^10	512 ± 6; 635 ± 29	123	23	1.432 ± 0.086; 0.304 ± 0.094	1.736 ± 0.127

For the evaluation of HNC and HCN populations from absorption profiles measured using the EC-QCL setup, we used the A_{jk} parameters from the ExoMol[5] and HITRAN2020[6] databases, respectively, and determined the n_j populations according to Eq.1. For the [HNC]/[HCN] abundance ratio determinations, we relied on the populations of HCN from the comb measurements and the EC-QCL measurements for HNC. In a first approach, we used the population of n_{20} (for R(J = 20) transition) of both HNC and HCN, utilizing the broad bandwidth of the comb that allows for state-to-state correlation, and hence accurate determination of the abundance ratio of the two species.

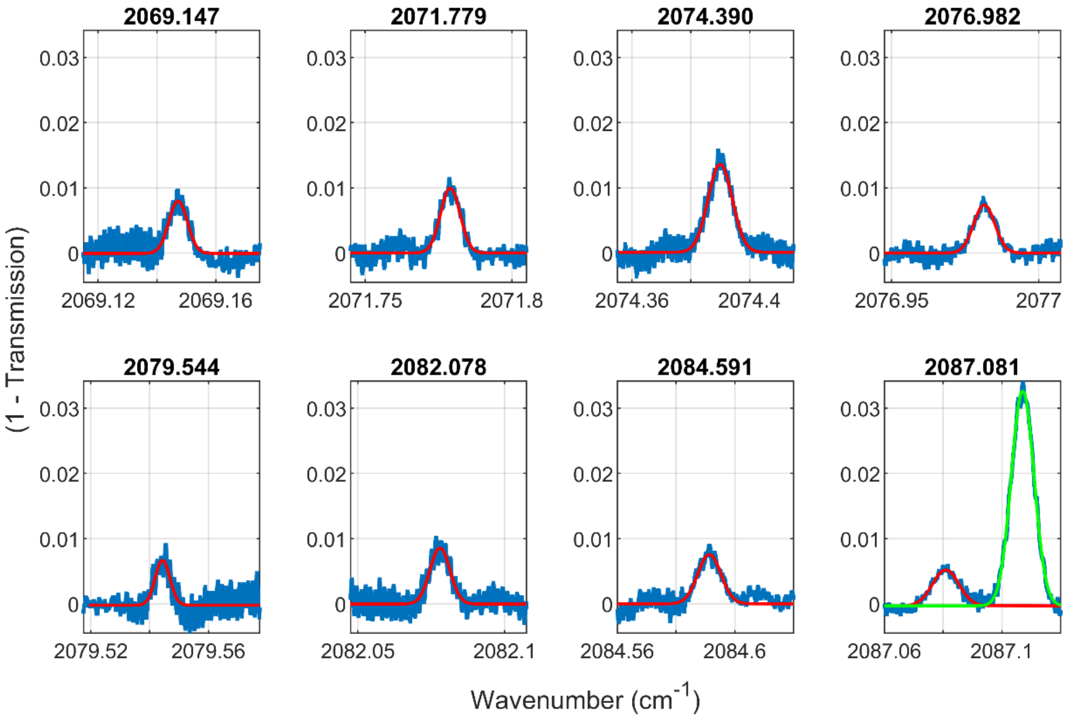

Fig. S3. Zoomed-in windows of measured absorption profiles of HNC (blue) together with a Gaussian line shape function fit (red). For the last panel a nearby HCN line, located at 2087.1 cm^{-1} (Gaussian fit, green) is also shown.

Additionally, we evaluated the rotational temperature for the ν_0 state of HNC from the measured transitions by the EC-QCL setup and then determined the total population of the ν_0 state. Fig. S3 shows zoomed-in windows of measured rovibrational profiles of HNC in the 2069 – 2087 cm^{-1} spectral region, which we used to create a Boltzmann plot and determine the rotational temperature. We have excluded the HNC line centered around 2074.390 cm^{-1}, because it is overlapping with a weak line of a hot band transition of CO_2, and the line centered around 2087.081 cm^{-1} because of the nearby HCN line that partially overlapped with it. From a linear fit of the remaining populations, we evaluated a rotational temperature of 846 ± 498 K for the ν_0 state of HNC, using the approach of Boltzmann plot (see Fig. S4). The large uncertainty in the evaluated rotational temperature is attributed to the low signal-to-noise ratio of measured profiles.

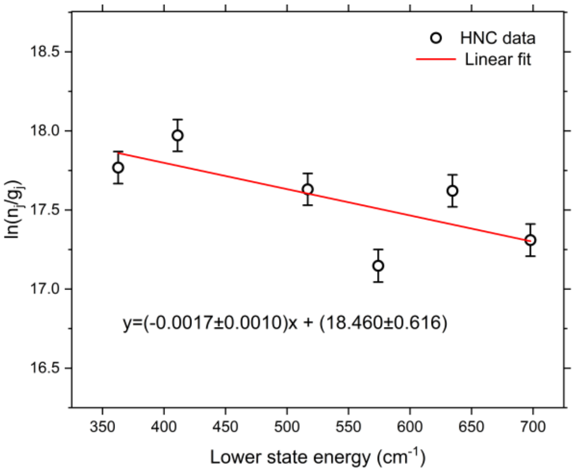

Fig. S4 Constructed Boltzmann plot of the measured HNC rotational populations, shown as, shown as ln(n_j/g_j) versus the lower state energy. Here, n_j is the population of the lower rotational level j of HNC derived from six transitions listed in Table 1 (main text), and g_j is the corresponding statistical weight. The solid red line represents a linear fit to the data, described by $y = (-0.0017\pm0.0010)x + (18.460\pm0.616)$, where y = ln($n_j/g_j$) and x = lower state energy. The fitted slope was used to determine the rotational temperature. The relatively large uncertainty in the fitted temperature reflects the limited signal-to-noise ratio of the measured absorption profiles.

Using the measured n_j populations and the determined rotational temperature in Eq. 2 and Eq. 4 (with the partition function of HNC),[4] we determined the total population of the ν_0 state of HNC. In another approach for evaluating the population of HNC in the ν_0 state, we assumed a similar dual T_{rot} distribution as was measured for HCN by the OFC-FTS. Using the measured n_j, e.g., for the R(20) of HNC, and applying Eq. 5 with same two T_{rots} of the ν_0 state of HCN, but with the segmented partition sums for HNC, we evaluated a total ν_0 population of HNC ($n_{0,1} + n_{0,2}$). The results of the determined populations are listed in Table 2 in the main text.

(i) Cross-check of HCN lower-state populations

To verify the internal consistency of the population analysis for HCN, we compared lower-state populations derived independently from EC-QCL and OFC-FTS measurements for two well-resolved rovibrational transitions, P(5) and P(11), originating from the ground vibrational state.

The EC-QCL measurements provide high-resolution measurements in the spectral region where strong HNC absorption occurs but also capture HCN transitions (see Fig. 3 in the main text The OFC-FTS measurements, in contrast, cover a broadband spectrum, allowing the simultaneous determination of hundreds of transitions of HCN but the transitions of HNC in the comb range are relatively weak and are not captured in the comb spectrum. For transitions that could not be measured directly due to saturation (as is the case for low-J transitions in the ν_1 band of HCN, see Fig. 2a), the constructed Boltzmann plot of the rotational populations (from measured unsaturated transitions) allows extrapolation to determine these populations reliably. Table S2 summarizes the spectroscopic parameters (e.g., A_{jk}, ν_{jk}, g_j, g_k), and the fit results for the P(5) and P(11) transitions used to calculate the lower-state populations derived from both EC-QCL and OFC-FTS measurements. The relative difference (Δ) is normalized to the average of the two populations. The comparison shows that the populations derived from EC-QCL and OFC-FTS measurements agree within 24–30%, which is reasonable given the independent measurement techniques and the extrapolation applied to partially saturated transitions.

Table S2. Comparison of HCN lower-state populations from EC-QCL and OFC-FTS measurements for P(5) and P(11) transitions. Populations from comb measurements were obtained by extrapolating the Boltzmann plot for saturated transitions. Δ is the relative difference normalized to the average of the two populations.

	ν_{ik} [cm^{-1}]	Int. area [10^7 cm^{-2}]	FWHM [cm^{-1}]	g_k	g_j	A_{jk} [s^{-1}]	n_j(QCL) [10^{13} cm^{-3}]	n_j (OFC) [10^{14} cm^{-3}]	Δ
P(5)	2081.86622	1.6893	0.00749	54	66	0.00769	8.7679	1.1167	0.24
P(11)	2081.32901	2.2139	0.00827	126	138	0.00797	9.9301	1.3400	0.30

An additional internal cross-check of the population analysis is performed by comparing vibrational populations of HCN obtained using two different approaches: (i) the bimodal non-LTE rotational temperature analysis, and (ii) vibrational populations inferred assuming thermal equilibrium at the gas kinetic temperature derived from Doppler linewidths. Table S1 lists the vibrational populations of the HCN bending mode determined from the OFC-FTS measurements using the bimodal non-LTE approach. From these populations, an effective vibrational temperature of 993 ± 68 K is obtained, indicating significant vibrational–rotational non-equilibrium.

For comparison, vibrational populations were also evaluated assuming LTE at the gas kinetic temperature $T_{\mathrm{gas}} = 507 \pm 37$ K, derived from Doppler widths of HCN absorption lines measured with the OFC-FTS. Using Eqs. (2) and (3), the population of the vibrational ground state n_{υ_0} was derived from a set of nine well-resolved rovibrational transitions. The resulting values are summarized in Table S3, yielding an average ground-state population of $n_{\upsilon_0} = (5.62\pm0.26)\times10^{15}$ cm^{-3}. This value can be compared with the ground-state vibrational population obtained from the bimodal non-LTE analysis, $(4.55\pm0.09) \times 10^{15}$ cm^{-3} (Table S1). The agreement between the two values is reasonable, given that non-equilibrium effects are expected to be more pronounced for higher vibrational states and hot-band populations than for the vibrational ground state. Overall, this comparison provides an additional internal consistency check and supports the robustness of the population analysis used in method (iv) for abundance ratio [HNC]/[HCN].

Table S3. Rotational-state populations n_j, lower-state energies E_j, Boltzmann factors $\phi(j,T)$ evaluated at the gas kinetic temperature T_{gas}= 507, and the corresponding vibrational ground-state populations n_{υ_0} of HCN derived assuming thermal equilibrium.

J	n_j [10^{13} cm^{-3}]	E_j [cm^{-1}]	$\phi(j,T)$	n_{υ_0} [10^{15} cm^{-3}]
33	0.352	1654.91	0.000663	5.32
32	0.460	1557.76	0.000849	5.43
31	0.589	1463.54	0.001077	5.47
30	0.745	1372.23	0.001353	5.50
29	0.919	1283.85	0.001685	5.46
28	1.170	1198.40	0.002079	5.64
27	1.460	1115.87	0.002539	5.73
26	1.830	1036.279	0.003072	5.95
25	2.250	959.6158	0.00368	6.10

C. Analytical model for [HNC]/[HCN] abundance ratio

In contrast to the near-unity [HNC]/[HCN] abundance ratio often observed in cold interstellar environments, we measured an abundance ratio in the order of ~ 10^{-4} in our molecular plasma experiment. We developed a simple analytical model based on the kinetic schematic in Fig. 5 of the main text. It incorporates formation via both excited and cold channels, unimolecular isomerization, cooling via relaxation, and destruction and conversion processes (e.g., catalytic isomerization via reactions with reactive M = C, H, or O available in the plasma) for HNC in ground states. The key processes involve:

(i) 'hot' and 'cold' formation pathways

The formation of internally excited intermediates, denoted with "*", is typically taking place through exothermic reactions that store a considerable fraction of exothermicity as internal energy for subsequent isomerization or other fast processes, before being relaxed to the ground state. Formation of 'cold' isomers can take place through endothermic reactions or exothermic reactions that have exothermicity lower than the isomerization barrier. Table S4 lists chemical reactions relevant to the formation, dissociation, and interconversion of HCN and HNC, together with their relative energies. A comprehensive list of other chemical reactions involving HCN and HNC formation, particularly relevant to interstellar media, can be found in the Supporting Materials of Ref. [7] In the list of Table S4, reactions R1–R9 involve the formation of *hot intermediates*, as they are associated with significant exothermicity — here approximated by the relative energy, evaluated as the difference in energy between reactants and products — exceeding the isomerization barrier of 186 kJ/mol. Among these, R9 is particularly relevant to interstellar environments. On the other hand, R10 is particularly relevant to thermal processes for HCN syntheses of conventional thermal nitrocarburizing without plasmas. R11 represents a case of *selective formation*, producing hot HNC* and cold HCN. In contrast, reactions R12–R16 lead to the formation of 'cold' intermediates, i.e., species with internal energy below the isomerization barrier. R17 is both thermodynamically and kinetically efficient,[8] and it facilitates the conversion of HNC to HCN.

Table S4. Chemical reactions and their relative energies relevant to HCN and HNC formation in molecular plasmas.

Reaction				**ΔE_{rel} [kJ/mol]**	**Ref**
R1	$H + H_2CN$	→	$HCN^* + H_2$	–331	[9]
		→	$HNC^* + H_2$	–276	
R2	$C + NH_2$	→	$HNC^* + H$	–499	1,[10, 11]
R3	$N + CH_2$	→	$HCN^* + H$	–510	1,[10, 11]
R4	$CH + NH$	→	$HCN^* + H$	–599	[12]
		→	$HNC^* + H$	–-546	
R5	$C + H_2CN$	→	$HCN^* + CH$	–234	[7]
R6	$C + CH_2NH$	→	$HCN^* + CH_2$	–264	[7]
R7	$N + H_2CN$	→	$HCN^* + NH$	–229	[9]
R8	$N + H_2CCN$	→	$HCN^* + HNC$	–403	[7]

R9	$HCNH^+ + e^-$	→	$HCN^* + H$	–596	[13]
		→	$HNC^* + H$	–543	
R10	$NH_3 + C$	→	$HCN + H_2$	9.15	[14]
R11	$CH_2 + NH$	→	$HCN + 2H$	–175	[7]
		→	$HNC^* + H_2$	–558	
R12	$N + CH_3$	→	$HCN + 2H$	–48	[9]
R13	$N + C_2H$	→	$HCN + C$	–187	[8]
		→	$HNC + C$	–132	
R14	$H + C_2N$	→	$HCN + C$	–55	[8]
R15	$CH + HCN$	→	$CCN + H_2$	–42	[15, 16]
		→	$HCCN + H$	–23	
R16	$CH + HNC$	→	$CCN + H_2$	–97	[9]
		→	$HCCN + H$	–76	
R17	$C + HNC$	→	$HCN + C$	–53	[8]

For reactions that involve internally exited intermediates, the formed HCN^* and HNC^* will rapidly isomerize on a sub-picosecond scale, establishing a pre-equilibrium: $\mathrm{HNC}^* \rightleftharpoons \mathrm{HCN}^*$. We denote the total formation rate of excited intermediates as: $P^* = P_{HNC^*} + P_{HCN^*}$, this gives:

$$[\mathrm{HNC}^*] = [\mathrm{HCN}^*] = \frac{P^*}{2(k_{\mathrm{rel}} + k^*_{\mathrm{diss}} + k^*_{\mathrm{conv}})} \qquad (6)$$

Where, k_{rel}, k^*_{diss}, and k^*_{conv} are the respective relaxation, destruction, and interconversion (i.e., catalytic isomerization) rates of formed hot intermediates. We also define β as the fraction of HCN and HNC from the hot pathway, and hence $(1- \beta)$ is the cold-pathway fraction. For the cold pathway, we define $P_0 = P_{HCN} + P_{HNC}$ as the total cold formation rate, with γ being the fraction of cold formation producing HCN, and $(1- \gamma)$ for HNC, although the latter is expected to be very minor because of the high energy of HNC.

(ii) Effective relaxation efficiencies:

Excited species may relax to the ground state, dissociate, or undergo chemical reactions before cooling. These processes compete with fast isomerization and become very significant when the system approaches the isomerization barrier, where the isomerization rate slows down. Under plasma conditions, relaxation typically takes place via collisions (molecular or with surfaces) within a relatively short time ($\sim 10^{-4} – 10^{-5}$ s at 1 mbar for polar molecules such as HCN when colliding with N_2, O_2, and CO[17]). Relaxation is predicted to be even faster for self-collisions of these polar molecules. This contrasts relaxation in molecular clouds, which takes place radiatively and is relatively slow $\sim 10^{-2}$ s. To account for such competing processes as molecules relax down the potential energy levels, we define effective relaxation efficiencies:

$$\eta_{\mathrm{HNC}^*} = \frac{k_{\mathrm{rel}}^{\mathrm{HNC}^*}}{k_{\mathrm{rel}}^{\mathrm{HNC}^*} + k_{\mathrm{diss}}^{\mathrm{HNC}^*} + k_{\mathrm{conv}}^{\mathrm{HNC}^*}} \qquad (7)$$

$$\eta_{\mathrm{HCN}^*} = \frac{k_{\mathrm{rel}}^{\mathrm{HCN}^*}}{k_{\mathrm{rel}}^{\mathrm{HCN}^*} + k_{\mathrm{diss}}^{\mathrm{HCN}^*} + k_{\mathrm{conv}}^{\mathrm{HCN}^*}} \tag{8}$$

Here, $k_{\mathrm{conv}}^{\mathrm{HNC}^*}$ and $k_{\mathrm{conv}}^{\mathrm{HCN}^*}$represent the conversion rates of HNC^* to HCN^* and vice versa by *catalytic isomerization* reactions of the form $\mathrm{HNC}^* + \mathrm{M} \rightleftharpoons \mathrm{HCN}^* + M$, where M denotes catalytic species such as C, H, or O atoms in the plasma. Note that any conversion or dissociation process occurring while the intermediates possess internal energy higher than the isomerization will generally be offset by the rapid unimolecular isomerization. However, near the isomerization barrier, these competing rates begin to favor the accumulation of one isomer over the other, most likely the more thermodynamically stable HCN.

(iii) Post-relaxation fate of ground-state isomers:

Relaxed isomers from the hot pathway, as well as directly formed cold isomers, can further undergo dissociation. Both isomers can dissociate via electron impact processes, surface losses, or reactions with background gas species. However, the highly reactive HNC isomer is expected to dissociate faster compared to HCN. Ground state HNC can still convert to HCN through catalytic reactions with atomic species such as C and H present in the plasmas. To describe this competition, we define an overall ground state destruction efficiency for HNC as:

$$\chi_{\mathrm{HNC}} = \frac{k_{\mathrm{diss}}^{\mathrm{HNC}}}{k_{\mathrm{diss}}^{\mathrm{HNC}} + k_{\mathrm{conv}}^{\mathrm{HNC}}} \tag{9}$$

For HCN, on the other hand, it is more appropriate to define stabilization efficiency as HCN tends to accumulate over time, as shown in Fig. 4 of the main text:

$$\chi_{\mathrm{HCN}} = \frac{k_{\mathrm{stab}}^{\mathrm{HCN}}}{k_{\mathrm{stab}}^{\mathrm{HCN}} + k_{\mathrm{diss}}^{\mathrm{HCN}}} \tag{10}$$

(iv) Final abundance ratio expressions:

Assuming a total production $P_{\mathrm{tot}} = 1$, so that the fraction of β forming via hot channels $\beta = P^*$, and $[\mathrm{HCN}^*] \approx [\mathrm{HNC}^*] \approx \beta/2$, due to the ultrafast equilibration. The remaining fraction, $P_0 = (1-\beta)$, corresponds to the cold pathway. Now, by collecting all contributions to final [HCN] and [HNC], we write:

$$[\mathrm{HCN}] = (1 - \chi_{\mathrm{HCN}}) \cdot \left[\frac{\beta}{2} \cdot \eta_{\mathrm{HCN}^*} + \gamma \cdot (1 - \beta)\right] + \theta \cdot \left[\frac{\beta}{2} \cdot \eta_{\mathrm{HNC}*} + (1 - \gamma) \cdot (1 - \beta)\right] \tag{6}$$

$$[\mathrm{HNC}] = (1 - \chi_{\mathrm{HNC}} - \theta) \cdot \left[\frac{\beta}{2} \cdot \eta_{\mathrm{HNC}^*} + (1 - \gamma) \cdot (1 - \beta)\right] \tag{7}$$

Here, $\frac{\beta}{2} \cdot \eta_{\mathrm{HCN}^*}$ and $\frac{\beta}{2} \cdot \eta_{\mathrm{HNC}^*}$ represent the contribution from hot intermediates for HCN and HNC, respectively. $\gamma \cdot (1 - \beta)$ and $(1 - \gamma) \cdot (1 - \beta)$ represent the contribution from the cold pathway. $(1 - \chi_{\mathrm{HCN}})$ in Eq. 6 represents the fraction of HCN stabilized. The second term in Eq. 6 involving θ accounts for cold HNC that is converted into HCN. The [HNC]/[HCN] abundance ratio can then be expressed as:

$$\frac{[\mathrm{HNC}]}{[\mathrm{HCN}]}=\frac{(1-\chi_{\mathrm{HNC}}-\theta)\cdot\left[\frac{\beta}{2}\cdot\eta_{\mathrm{HNC}^*}+(1-\gamma)\cdot(1-\beta)\right]}{(1-\chi_{\mathrm{HCN}})\cdot\left[\frac{\beta}{2}\cdot\eta_{\mathrm{HCN}^*}+\gamma\cdot(1-\beta)\right]+\theta\cdot\left[\frac{\beta}{2}\cdot\eta_{\mathrm{HNC}^*}+(1-\gamma)\cdot(1-\beta)\right]} \tag{8}$$

Simplified case I: When considering only hot formation pathway ($\beta = 1$), relevant to molecular plasmas:

$$\frac{[\mathrm{HNC}]}{[\mathrm{HCN}]}=\frac{(1-\chi_{\mathrm{HNC}}-\theta)\cdot\eta_{\mathrm{HHNC}^*}}{(1-\chi_{\mathrm{HCN}})\cdot\eta_{\mathrm{HCN}*}+\theta\cdot\eta_{\mathrm{HNC}^*}} \tag{9}$$

Simplified case II: When considering only the cold formation pathway ($\beta = 0$), relevant to conventional nitriding, nitrocarburizing, and thermal chemical production of HCN:

$$\frac{[\mathrm{HNC}]}{[\mathrm{HCN}]}=\frac{(1-\chi_{\mathrm{HNC}}-\theta)\cdot(1-\gamma)}{(1-\chi_{\mathrm{HCN}})\cdot\gamma+\theta\cdot(1-\gamma)} \tag{10}$$

The model shows that [HNC]/[HCN] ratio depends on an interplay between the key parameters: (i) η_{HNC^*} (stabilization efficiency of hot HNC), which determines how much HNC is formed from excited HNC^*; (ii) χ_{HNC} (destruction fraction of HNC), which governs how much HNC is destroyed before it accumulates; and (iii) θ (conversion fraction of HNC + M → HCN + M, with M = C, H, or O).

To reach an abundance ratio as low as 10^{-4}, the plasma must strongly favor the formation and stabilization of HCN over HNC. This scenario occurs when the relaxation efficiency of HNC^* (η_{HNC^*}) is low, meaning that excited HNC* rarely survives to become ground-state HNC. Moreover, even a fraction of HNC that does stabilize (quantified by θ) can be converted to HCN. Together with high χ_{HNC}, very small abundances of HNC can survive. As shown in the surface plots (Fig. 5: β-vs-η_{HNC^*} (right panel) and η_{HNC^*} vs. χ_{HNC} (left panel)), the lowest $\log_{10}$([HNC]/[HCN]) values appear at low η_{HNC^*} and moderate-high β. This suggests that while HNC^* may be produced in significant amounts, it rapidly dissociates before stabilizing. The surface is flat along the β direction when $\eta_{\mathrm{HNC}^*}$is low, indicating that if HNC^* cannot stabilize, its abundance remains negligible regardless of production rates — an outcome consistent with molecular plasma conditions. The η_{HNC^*} vs. $\chi_{\mathrm{HNC}}+\theta$ surface shows that when $\chi_{\mathrm{HNC}}+\theta\approx 1$, almost all HNC is destroyed. Here, θ not only reduces HNC, but also enhances HCN formation.

Ground-state HNC is particularly reactive and can be destroyed through various pathways, including reactions with atoms (e.g., H, C, O), and ionic (e.g., C^+, CH_3^+, and H_3^+), and other radicals (e.g., CH, $\mathrm{C_2H}$, and $\mathrm{C_2}$). For example, the reaction of HNC + C is barrierless or has only a small activation barrier (~few hundred Kelvin), proceeding at a near collision-limited rate (1.15×10^{-10} $\mathrm{cm^3}$ $\mathrm{molecule^{-1}}$ $\mathrm{s^{-1}}$).[8] Similarly, CH + HNC is exothermic and takes place at a rate of 1.40×10^{-10} $\mathrm{cm^3}$ $\mathrm{molecule^{-1}}$ $\mathrm{s^{-1}}$.[9] Many of these reactions converts HNC into HCN, boosting the latter's concentration while further suppressing the former. These rapid destruction mechanisms explain the significantly lower [HNC]/[HCN] ratios observed in plasma experiments compared to molecular cloud environments.

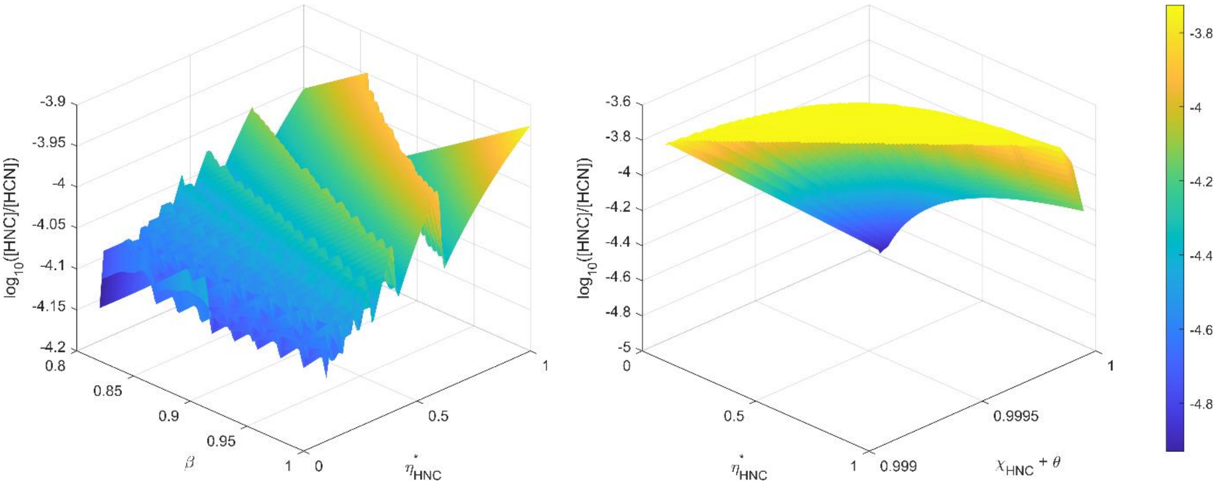

Fig. S5. Left panel: Surface plot of log$_{10}$([HNC]/[HCN]) as a function of β and η_{HNC^*}. The ratio remains extremely low at small η_{HNC^*}, regardless of β, highlighting the dominance of stabilization over mere production in excited-state chemistry. Right panel: Surface plot of log$_{10}$([HNC]/[HCN]) as a function of η_{HNC^*} and $\chi_{\mathrm{HNC}} + \theta$. The surface reveals strong suppression of HNC when both destruction (χ_{HNC}) and conversion (θ) are high, especially at low stabilization efficiency (η_{HNC^*}).

REFERENCE

1. I. Sadiek, A. Puth, G. Kowzan, A. Nishiyama, S.-J. Klose, J. Röpcke, N. Lang, P. Masłowski and J.-P. H. van Helden, *Plasma Sources Sci. Technol*, 2024, **33**, 075011.
2. I. Sadiek, A. J. Fleisher, J. Hayden, X. Huang, A. Hugi, R. Engeln, N. Lang and J.-P. H. van Helden, *Commun. Chem.*, 2024, **7**, 110.
3. M. Šimečková, D. Jacquemart, L. S. Rothman, R. R. Gamache and A. Goldman, *J. Quant. Spectrosc. Radiat. Transf.*, 2006, **98**, 130-155.
4. R. J. Barber, J. K. Strange, C. Hill, O. L. Polyansky, G. C. Mellau, S. N. Yurchenko and J. Tennyson, ExoMol line lists – III. *Mon. Not. R. Astron.*, 2013, **437**, 1828-1835.
5. J. Tennyson, S. N. Yurchenko, J. Zhang, C. A. Bowesman, R. P. Brady, J. Buldyreva, K. L. Chubb, R. R. Gamache, M. N. Gorman, E. R. Guest, C. Hill, K. Kefala, A. E. Lynas-Gray, T. M. Mellor, L. K. McKemmish, G. B. Mitev, I. I. Mizus, A. Owens, Z. Peng, A. N. Perri, M. Pezzella, O. L. Polyansky, Q. Qu, M. Semenov, O. Smola, A. Solokov, W. Somogyi, A. Upadhyay, S. O. M. Wright and N. F. Zobov, *J. Quant. Spectrosc. Radiat. Transf.*, 2024, **326**, 109083.
6. I. E. Gordon, L. S. Rothman, R. J. Hargreaves, R. Hashemi, E. V. Karlovets, F. M. Skinner, E. K. Conway, C. Hill, R. V. Kochanov, Y. Tan, P. Wcisło, A. A. Finenko, K. Nelson, P. F. Bernath, M. Birk, V. Boudon, A. Campargue, K. V. Chance, A. Coustenis, B. J. Drouin, J. M. Flaud, R. R. Gamache, J. T. Hodges, D. Jacquemart, E. J. Mlawer, A. V. Nikitin, V. I. Perevalov, M. Rotger, J. Tennyson, G. C. Toon, H. Tran, V. G. Tyuterev, E. M. Adkins, A. Baker, A. Barbe, E. Canè, A. G. Császár, A. Dudaryonok, O. Egorov, A. J. Fleisher, H. Fleurbaey, A. Foltynowicz, T. Furtenbacher, J. J. Harrison, J. M. Hartmann, V. M. Horneman, X. Huang, T. Karman, J. Karns, S. Kassi, I. Kleiner, V. Kofman, F. Kwabia–Tchana, N. N. Lavrentieva, T. J. Lee, D. A. Long, A. A. Lukashevskaya, O. M. Lyulin, V. Y. Makhnev, W. Matt, S. T. Massie, M. Melosso, S. N. Mikhailenko, D. Mondelain, H. S. P. Müller, O. V. Naumenko, A. Perrin, O. L. Polyansky, E. Raddaoui, P. L. Raston, Z. D. Reed, M. Rey, C. Richard, R. Tóbiás, I. Sadiek, D. W. Schwenke, E. Starikova, K. Sung, F. Tamassia, S. A. Tashkun, J. Vander Auwera, I. A. Vasilenko, A. A. Vigasin, G. L. Villanueva, B. Vispoel, G. Wagner, A. Yachmenev and S. N. Yurchenko, *J. Quant. Spectrosc. Radiat. Transf.*, 2022, **277**, 107949.
7. J.-C. Loison, V. Wakelam and K. M. Hickson, *Mon. Not. R. Astron. Soc.*, 2014, **443**, 398-410.
8. J. C. Loison and K. M. Hickson, *Chem. Phys. Lett.*, 2015, **635**, 174-179.
9. E. Hébrard, M. Dobrijevic, J. C. Loison, A. Bergeat and K. M. Hickson, *Astron. Astrophys.*, 2012, **541**, A21.

10. E. Herbst, R. Terzieva and D. Talbi, *Mon. Not. R. Astron. Soc.*, 2000, **311**, 869-876.
11. D. Talbi, *Chem. Phys. Lett.*, 1999, **313**, 626-632.
12. K. Takahashi and T. Takayanagi, *J. Mol. Struct. THEOCHEM*, 2007, **817**, 153-160.
13. J. Semaniak, B. F. Minaev, A. M. Derkatch, F. Hellberg, A. Neau, S. Rosen, R. Thomas, M. Larsson, H. Danared, A. Paal and M. af Ugglas, *Astrophys. J., Suppl. Ser.*, 2001, **135**, 275-283.
14. R. M. Badger, *J. Am. Chem. Soc.*, 1924, **46**, 2166-2172.
15. B. Du and W. Zhang, *Int. J. Quantum Chem.*, 2006, **106**, 1827-1843.
16. S. Zabarnick, J. W. Fleming and M. C. Lin, *Chem. Phys.*, 1991, **150**, 109-115.
17. G. S. Arnold and I. W. M. Smith, *J. Chem. Soc., Faraday Trans. 2; Chem. Phys.*, 1981, **77**, 861-871.